



## Regimes of steady jetting in electrohydrodynamic jet printing

Abhishek K. Singh <sup>1</sup>, Rajiv K. Srivastava <sup>2</sup>, and Supreet Singh Bahga<sup>1,\*</sup>

<sup>1</sup>*Department of Mechanical Engineering, Indian Institute of Technology Delhi, New Delhi 110016, India*

<sup>2</sup>*Department of Textile Technology, Indian Institute of Technology Delhi, New Delhi 110016, India*



(Received 6 October 2021; accepted 24 May 2022; published 6 June 2022)

We present an experimental and theoretical investigation of steady jetting regimes in the electrohydrodynamic (EHD) jet printing process, wherein a liquid jet issuing from a needle is stretched by applying a high electric field between the needle and a collector substrate. While EHD jetting is well understood in the context of the electrospray process, we show that the jetting characteristics can differ significantly in the printing configuration in which the needle is kept close to the collector to prevent spraying. Through experimental visualization of EHD jets and current measurements, we show that steady EHD jetting can occur in three regimes, namely, the cone-jet, moderately stretched jet, and thick-jet regimes, depending on the flow rate, applied potential difference, and needle-to-collector gap. To elucidate the underlying physics of these experimentally observed regimes, we perform order-of-magnitude analysis for the current transfer region of the jet, where the conduction and surface convection currents are of comparable magnitude. Based on the relative size of the current transfer region and the jet diameter, we derive the criteria for observing the three steady EHD jetting regimes. For each of these regimes, we also describe the dependence of the jet diameter and the current carried by jet on flow rate, potential difference, and aspect ratio in the form of scaling relations. The theoretical criteria for various steady jetting regimes and the corresponding scaling relations for the jet diameter and current show good agreement with the experimental observations. These theoretical relations can be useful for the design, performance monitoring, and control of EHD jet printing.

DOI: [10.1103/PhysRevFluids.7.063701](https://doi.org/10.1103/PhysRevFluids.7.063701)

### I. INTRODUCTION

Electrohydrodynamic (EHD) jet printing is an additive manufacturing technique in which an electrified jet of functional ink is deposited on a motion-controlled substrate [1]. Unlike other direct ink writing methods, EHD jet printing enables patterning of submicrometer resolution structures. Therefore, EHD jet printing has enormous potential in the fabrication of printed electronics [2–4], scaffolds for tissue engineering [5], optical microlenses [6], and micro-optical devices [7].

A typical EHD jet printer is illustrated in Fig. 1. A metallic needle having an inner diameter of  $O(0.1\text{--}1.0\text{ mm})$  is kept at a known distance from a large collector on which the features are to be printed. The gap between the needle tip and the collector is typically  $O(0.1\text{--}10\text{ mm})$ . A leaky-dielectric liquid [8] is flown through the needle at a flow rate of  $O(0.1\text{--}1.0\text{ ml min}^{-1})$ , and an electric field of  $O(10^6\text{ V m}^{-1})$  is applied by applying high potential on the needle and grounding the collector. Electrical conduction within the liquid leads to charge accumulation at the liquid interface, resulting in electrical stresses that stretch the liquid interface to form a thin jet. For a particular range of flow rate and potential difference, steady EHD jetting is observed [9]. At other

\*bahga@mech.iitd.ac.in

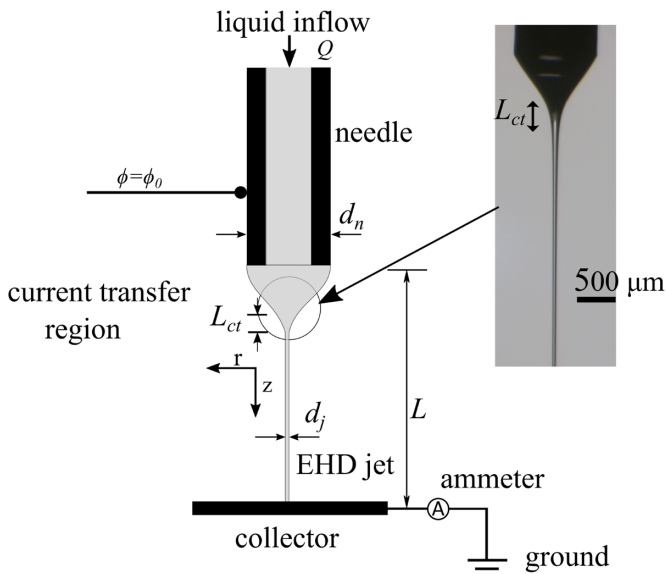


FIG. 1. Schematic illustration of an experimental setup in the EHD jet printing. A liquid jet issuing from the needle is stretched by applying a large potential difference between the needle and the collector. The current carried by the EHD jet is measured through a current measuring probe connected between the collector and the ground. Simultaneously, the jet is visualized through a horizontally mounted microscope.

conditions, liquid may flow from the needle in the form of dripping, pulsating jet, tilted jet, and multijet modes [10].

In the current work, we focus on steady EHD jetting, which is widely used for printing continuous features in EHD jet printing. Depending upon the flow rate and applied electric field, the steady jet may have a diameter ranging from the needle diameter to as small as two orders of magnitude smaller than the needle diameter [11]. In practice, it is difficult to visualize microscopic jet during the EHD jet printing process. Therefore, monitoring of the EHD jetting process during printing is often done using the electric current, which can be measured easily compared with real-time visualization of the jet [12]. Moreover, current measurement enables feedback control of jet characteristics by adjusting the flow rate and applied voltage difference. Therefore, it is essential to understand the scaling behavior of the jet diameter and current in various steady EHD jetting regimes. The total current carried by a typical cone jet comprises the current due to the conduction of free charge through the bulk liquid and surface convection of the charge accumulated at the liquid surface [13]. The conduction current dominates in the meniscus close to the needle tip, whereas the convection current dominates downstream where the conduction resistance is too high due to the small diameter of the jet. In the intermediate region separating the meniscus and the thin jet, the conduction and surface convection currents are of comparable magnitude. This intermediate region, shown in Fig. 1, is called the current transfer region [11]. Numerous experimental and theoretical studies have reported the dependence of jet diameter and the current on operational parameters such as flow rate and applied electric field [11, 14–25]. However, most of these studies pertain to the electrospray process, wherein the gap between the needle and the collector is relatively large compared with the needle diameter. In contrast, the needle-to-collector distance in EHD jet printing is comparable to the needle diameter, as illustrated in Fig. 1, to prevent the jet from breaking up into a spray. Therefore, the scaling laws for jet diameter and current carried by an electrified jet in the electrospray process need not be applicable for the EHD jet printing process.

In the current work, we present a detailed experimental investigation of various regimes of steady EHD jetting in the printing process and the scaling behavior of jet diameter and current

TABLE I. Physical properties of the working liquids. Also provided are the reference scales for various quantities used for nondimensionalization and the dimensionless numbers.

Liquid	$\rho$ (kg m <sup>-3</sup> )	$\mu$ (mPa s)	$\gamma$ (mN m <sup>-1</sup> )	$k$ ( $\mu$ S m <sup>-1</sup> )	$Q_0$ ( $\mu$ l min <sup>-1</sup> )	$\phi_0$ (V)	$I_0$ (nA)	$d_0$ ( $\mu$ m)	$\epsilon_r$	$Re_0$
1-octanol	825.5	8.0	26	1.16	14.40	189.6	2.7	12.2	10.3	2.0
1-butanol	800.0	2.5	23	7.50	2.03	94.2	2.4	3.4	17.8	3.1

in these regimes. We focus on EHD jetting dominated by inertia and tangential electric force, which typically occurs for low-viscosity and low-permittivity liquids. Through experimental observations and theoretical scaling analysis, we show that EHD jetting in the printing configuration occurs in three distinct regimes, namely, cone-jet, moderately stretched jet and thick-jet regimes. Based on order-of-magnitude estimations, we provide the operating conditions in terms of applied potential, flow rate, and aspect ratio (ratio of the needle-to-collector distance to the outer diameter of the needle) for jetting to occur in these three regimes. We also provide the scaling laws for jet diameter and current in these three regimes and validate them with experimental data. We begin by presenting the experimental methodology and observations in Sec. II. Section III presents the theoretical scaling analysis and validation of the scaling relations with experimental data. Section IV describes the range of validity of the scaling relations, and Sec. V provides the concluding remarks. These scaling laws show that the three EHD jetting regimes differ with respect to the relative importance of surface convection and bulk conduction currents downstream of the jet.

## II. EXPERIMENTAL

We performed a large set of experiments to visualize the EHD jetting phenomenon in the printing configuration and measured the emitted current for varying operating and geometrical parameters. To this end, we systematically varied the flow rate  $Q$ , applied potential difference  $\phi$  and aspect ratio  $\chi$  and measured the current carried by the electrified jet while simultaneously visualizing the jet. In this section, we discuss the experimental setup and present the experimental data for current carried by the jet and the jet diameter for varying operating conditions. We also identify the various regimes of EHD jetting in terms of the dimensionless numbers that govern the process.

### A. Experimental setup

Figure 1 shows a schematic of the experimental setup used to investigate the EHD jetting phenomenon. A 35 mm long stainless-steel needle with an inner diameter of 0.66 mm and an outer diameter of 1.0 mm was mounted on a vertical axis translation stage, and a metallic collector was placed perpendicular to the needle at a controllable distance from the needle tip. We performed experiments with two liquids, 1-octanol and 1-butanol (CDH India, AR grade). The relevant physical properties of these liquids are provided in Table I. The working liquid was flown through the needle at a constant flow rate using a syringe pump (KD Scientific, Legato 180). A variable high-voltage power supply (Keithley-2290-10) was used to apply a potential difference between the needle and the collector. The jetting phenomenon was visualized using a horizontally mounted stereo-zoom microscope (Radical Scientific, 8–50 $\times$  zoom) equipped with a CMOS camera (Radical Scientific, Procam HS-5). The current carried by the EHD jet was measured using a laboratory-made setup consisting of precision operational amplifiers (op-amps). The current carried by the EHD jet was fed to the inverting terminal of the op-amp (OPA227P, Texas Instruments), and the voltage drop across a shunt resistor (1–10 M $\Omega$ , Texas Instruments) was measured using a multimeter (HP Hewlett Packard 34401a, precision 10<sup>-6</sup> mV). Subsequently, the total emitted current was estimated using  $I = V_s/R_s$ , where  $R_s$  is the resistance of the shunt resistor and  $V_s$  is

the measured voltage drop across the shunt resistor. High accuracy in current measurements was ensured by grounding the noninverting terminal of the op-amp through another precision op-amp (MCP601, Texas Instruments). At high flow rates, where the current is significantly high, the current was measured directly by measuring the voltage drop across the shunt resistor (10–30 k $\Omega$ ) without using the op-amps while ensuring the same precision and accuracy. The diameter of the EHD jet was measured by processing the microscopy images in MATLAB. All experimental measurements of jet diameter were made at a distance of  $0.85L$  from the needle tip, where  $L$  is the needle tip to collector distance in EHD jet printing. All the experiments were repeated five times at every operating condition. The random uncertainties in current and jet diameter were estimated using the  $t$  distribution. The total uncertainty in the current measurements was dominated by the random uncertainty, which was less than 3%. On the other hand, for diameter measurements, the systematic uncertainty due to pixel size of the camera sensor (2.2  $\mu\text{m}$ ) contributed significantly to the total uncertainty. The total uncertainty in diameter measurements obtained by combining systematic and random uncertainties [26] was less than 5% of the mean diameter.

### B. Dimensionless numbers

The behavior of EHD jet is governed by various dimensional parameters grouped into the following three categories: (i) operating parameters such as the flow rate  $Q$  and the potential difference  $\phi$ , (ii) geometrical parameters such as the outer diameter of the needle  $d_n$  and distance between needle tip to collector  $L$ , and (iii) physical properties of liquid such as density  $\rho$ , dynamic viscosity  $\mu$ , surface tension  $\gamma$ , electrical conductivity  $k$ , permittivity of liquid  $\epsilon$ , and vacuum  $\epsilon_0 = 8.85 \times 10^{-12}$  F m $^{-1}$ . It is convenient to group these ten dimensional parameters into the following six dimensionless groups:

$$\tilde{Q} = \frac{Q}{Q_0}, \tilde{\phi} = \frac{\phi}{\phi_0}, \chi = \frac{L}{d_n}, \frac{d_n}{d_0}, \epsilon_r = \frac{\epsilon}{\epsilon_0} \text{ and } \text{Re}_0 = \frac{\rho Q_0}{\mu d_0}. \quad (1)$$

Here  $Q_0$ ,  $d_0$ , and  $\phi_0$  defined by

$$Q_0 = \frac{\gamma \epsilon_0}{\rho k}, \quad d_0 = \left( \frac{\gamma \epsilon_0^2}{\rho k^2} \right)^{1/3}, \text{ and } \phi_0 = \left( \frac{\gamma d_0}{\epsilon_0} \right)^{1/2} \quad (2)$$

are the reference scales for flow rate, jet diameter, and potential difference, respectively. A detailed derivation of these reference scales has been provided by Higuera [18] by performing an order-of-magnitude analysis in the cone-to-jet transition region. Briefly, an order-of-magnitude balance between the pressure variation in inertia-dominated flow and surface tension force, to ensure departure from a steady Taylor cone, yields  $\rho v_0^2 = \gamma/d_0$ . Here  $v_0 = Q_0/d_0^2$  is the reference velocity scale. The balance between surface tension force and normal electric stress yields  $\phi_0 = \sqrt{\gamma d_0/\epsilon_0}$ . Finally, upon balancing the conduction and surface convection currents we arrive at the reference scales  $Q_0$  and  $d_0$ , given by Eq. (2). The dimensionless jet diameter,  $\tilde{d} = d/d_0$ , and the total dimensionless current carried by the electrified jet,  $\tilde{I} = I/I_0$ , where  $I_0 = \sqrt{(\epsilon_0 \gamma^2/\rho)}$ , depends on these six dimensionless groups,

$$\tilde{I}(\text{or } \tilde{d}) = f(\tilde{Q}, \tilde{\phi}, d_n/d_0, \chi, \epsilon_r, \text{Re}_0). \quad (3)$$

This equation suggests that, for a given liquid and fixed needle diameter, the total current carried by the electrified jet and its diameter depend only on the dimensionless flow rate  $\tilde{Q}$ , dimensionless potential difference  $\tilde{\phi}$ , and aspect ratio  $\chi$ . Therefore, for a given fluid, we performed the experiments by varying  $\tilde{Q}$ ,  $\tilde{\phi}$ , and  $\chi$  while keeping the needle diameter fixed. We performed experiments with two liquids, 1-octanol and 1-butanol. Table I provides the physical properties, corresponding reference scales, and dimensionless numbers for these liquids.

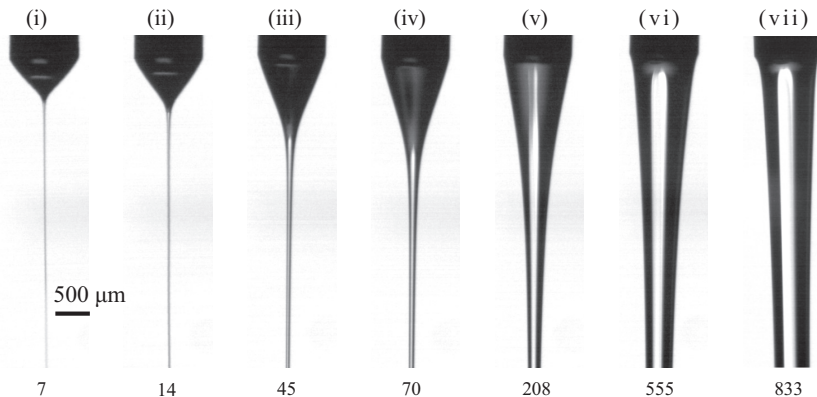


FIG. 2. Jetting behavior for 1-octanol at various dimensionless flow rates  $\tilde{Q}$ , at a fixed dimensionless potential difference  $\tilde{\phi} = 22.2$  and aspect ratio  $\chi = 6$ . Here  $\tilde{Q} = Q/Q_0$  and characteristic flow rate  $Q_0 = \gamma\epsilon_0/\rho k = 14.4 \mu\text{l min}^{-1}$ .

### C. Experimental observations for 1-octanol

#### 1. Current vs flow rate characteristics

First, we present experiments with 1-octanol to elucidate the effect of varying the flow rate on the steady jet shape and the emitted current at different values of applied potential difference. In these experiments, we varied the dimensionless flow rate  $\tilde{Q}$  between 4 and 833 for different values of dimensionless applied potential difference  $\tilde{\phi}$  and aspect ratio  $\chi$ . We note that for a given aspect ratio, the range within which  $\tilde{\phi}$  can be varied to achieve steady jetting is rather small compared with the range over which  $\tilde{Q}$  can be varied. Figure 2 shows the snapshots of the EHD jet for varying values of  $\tilde{Q}$  at  $\tilde{\phi} = 22.2$  and  $\chi = 6$ . At low flow rates, such as at  $\tilde{Q} = 7$ , the well-known Taylor cone-jet forms. The cone jet is characterized by a liquid cone attached to the needle with a fine jet streaming from the cone's tip. The diameter of this jet attains an asymptotic value shortly downstream of the conical meniscus. Figure 2 shows that the cone height and jet diameter increase upon increasing the flow rate until a limit is reached beyond which the cone and jet are indistinguishable. At high flow rates, such as at  $\tilde{Q} = 833$ , the jet diameter is almost equal to the needle diameter. Figure 3(a) shows the variation of the measured dimensionless current  $\tilde{I}$  with a dimensionless flow rate  $\tilde{Q}$  of 1-octanol for two aspect ratios ( $\chi = 3, 6$ ) and varying values of dimensionless potential difference  $\tilde{\phi}$ . We observe that at low flow rates ( $\tilde{Q} \lesssim 40$ ), the current  $\tilde{I}$  scales as  $\tilde{I} \sim \tilde{Q}^{1/2}$ , which is the well-known current-flow rate scaling for the Taylor cone-jet mode shown in Fig. 2(i) and 2(ii). This square root dependence of the current on the flow rate in the cone-jet regime is universal and independent of the needle and collector geometries, as discussed by Fernández de la Mora [19]. The data presented in Fig. 3(b) also show that at low flow rates where  $\tilde{I} \sim \tilde{Q}^{1/2}$ , the diameter of the jet also scales with the square root of the flow rate,  $\tilde{d} \sim \tilde{Q}^{1/2}$ , and remains independent of the  $\tilde{\phi}$  and  $\chi$ . Such square root dependence of the jet diameter on the flow rate is also a characteristic of the Taylor cone-jet regime [14].

Next, from Fig. 3(a) we observe that at high flow rates,  $\tilde{Q} \gtrsim 500$ , the measured current shows a weak dependence on  $\tilde{Q}$ . In particular, at high flow rates and low values of  $\tilde{\phi}$ , the current is almost independent of flow rate, as shown in the inset of Fig. 3. Moreover, the magnitude of the current is higher at low aspect ratios. We note that this scaling is observed for the same flow rates at which the jet is thick, and the jet diameter is similar to the needle diameter, as shown in Fig. 2(vi) and 2(vii).

Apart from the cone-jet regime at low flow rate and the thick-jet regimes at high flow rates, respectively, the experimental data presented in Fig. 3 for 1-octanol suggest a distinct jetting regime at intermediate flow rates,  $40 \lesssim \tilde{Q} \lesssim 500$ . As shown in Fig. 2(iii) and 2(iv), for these flow rates, the jet is moderately stretched, and the cone transitions smoothly to the jet, unlike in the cone-jet mode.

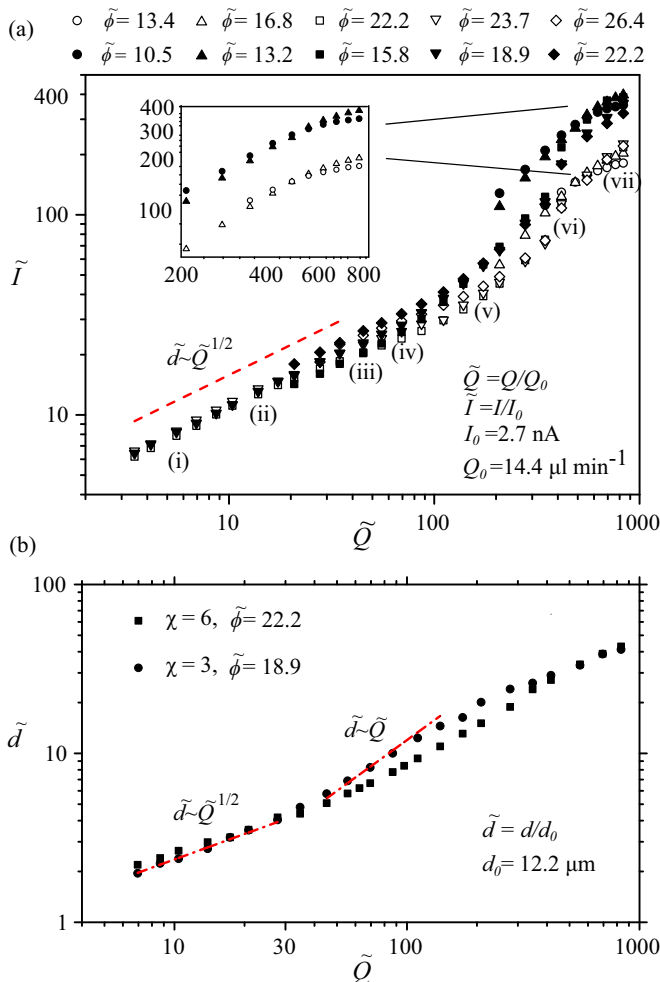


FIG. 3. Variation of current and jet diameter of an EHD jet of 1-octanol for varying values of flow rate and aspect ratio. (a) Log-log plot of the dimensionless current  $\tilde{I}$  for varying dimensionless flow rate  $\tilde{Q}$ . At  $\tilde{Q} \lesssim 40$ , the current scales as  $\tilde{I} \sim \tilde{Q}^{1/2}$ , whereas at  $\tilde{Q} \gtrsim 500$ , the current weakly depends on flow rate. Here (i) to (vii) correspond to the conditions for which snapshots of the jet are shown in Fig. 2. Inset of (a) shows  $\tilde{I}$  vs  $\tilde{Q}$  for low values of  $\tilde{\phi}$ , wherein current is nearly independent of flow rate for  $\tilde{Q} \gtrsim 500$ . Here hollow and filled symbols correspond to  $\chi = 6$  and  $\chi = 3$ , respectively. (b) Log-log plot of the dimensionless jet diameter  $\tilde{d}$  for varying  $\tilde{Q}$  at different values of  $\tilde{\phi}$  and  $\chi$ . The jet diameter increases monotonically with flow rate, and at high  $\tilde{Q}$  it tends to a constant value. Moreover, at flow rates,  $\tilde{Q} \lesssim 40$ , the jet diameter increases with the square root of the  $\tilde{Q}$ , whereas at  $\tilde{Q} \gtrsim 40$ , the jet diameter linearly increases with  $\tilde{Q}$ .

Moreover, in this regime, the jet diameter scales as  $\tilde{d} \sim \tilde{Q}$ . The current carried by jet increases with the flow rate and depends on the applied voltage and aspect ratio.

## 2. Current vs voltage characteristics

To further explore the differences between the various regimes of steady EHD jetting in the printing configuration, we systematically explored the current vs voltage characteristics for varying values of  $\tilde{Q}$  while simultaneously visualizing the jet of 1-octanol. For these set of experiments, we fixed the aspect ratio at  $\chi = 4$  and measured the current carried by jet for varying  $\tilde{\phi}$  at different

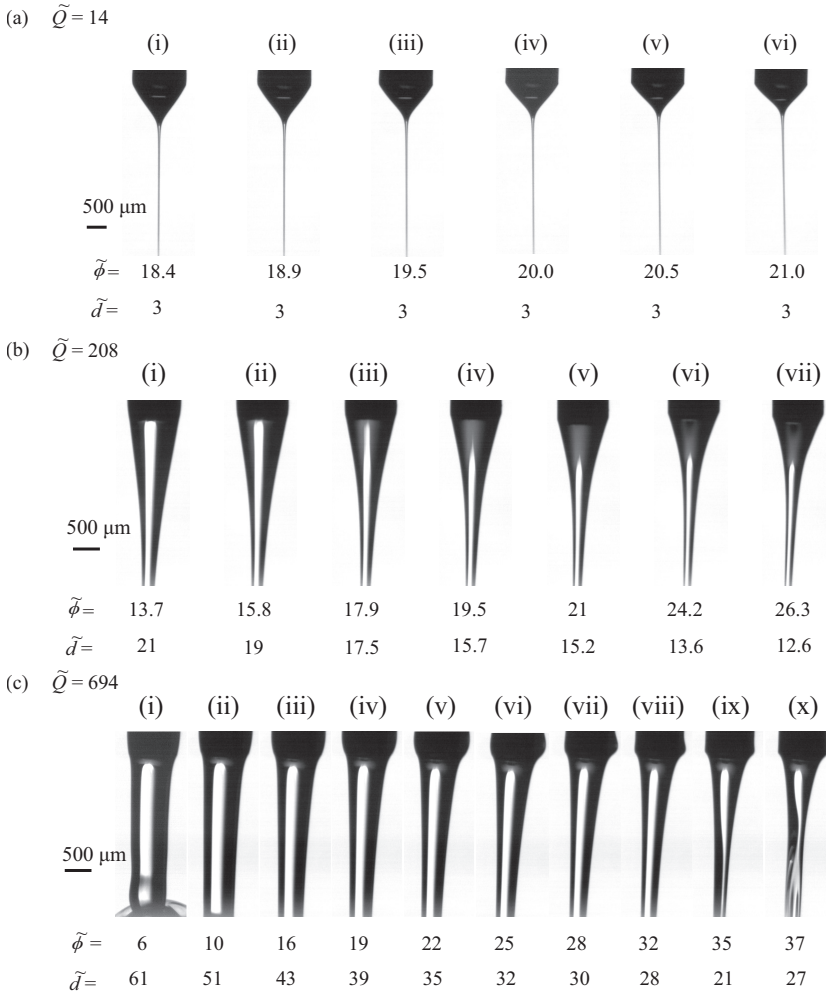


FIG. 4. EHD jetting behavior of 1-octanol for varying values of potential difference  $\tilde{\phi}$  at three flow rates: (a)  $\tilde{Q} = 14$ , (b)  $\tilde{Q} = 208$ , and (c)  $\tilde{Q} = 694$ . The cone-jet regime is observed at low flow rate  $\tilde{Q} = 14$ . The jet is moderately stretched at intermediate flow rate ( $\tilde{Q} = 208$ ) and at high flow rate with high  $\tilde{\phi}$ . At high flow rate and low potential difference, the jet diameter is almost equal to the diameter of the needle.

values of  $\tilde{Q}$ . Figure 4 shows the snapshots of the EHD jets for varying dimensionless potential difference  $\tilde{\phi}$  at three different flow rates,  $\tilde{Q} = 14$ , 208, and 694. Figure 4(a) shows that at  $\tilde{Q} = 14$  the shape of the jets is similar to the conventional Taylor cone jet, characterized by a very fine jet with anchored conical meniscus at the outlet of a needle. The cone-jet shape remains almost unchanged upon varying  $\tilde{\phi}$ , and the only visible change is the reduction in cone height upon an increase in  $\tilde{\phi}$ .

At an intermediate flow rate of  $\tilde{Q} = 208$ , the jet is moderately stretched, but it still attains an asymptotic shape downstream near the collector. However, in contrast to the cone-jet mode, the cone-to-jet transition is not localized and the jet shape varies appreciably with the applied potential difference, as shown in Fig. 4(b). In particular, the transition region connecting the jet and the cone becomes smaller upon increasing  $\tilde{\phi}$ . Figure 4(c) shows that, at very high flow rates, such as at  $\tilde{Q} = 694$ , the jet is thick ( $d \approx d_n$ ) at low values of  $\tilde{\phi}$ . However, as the applied potential is

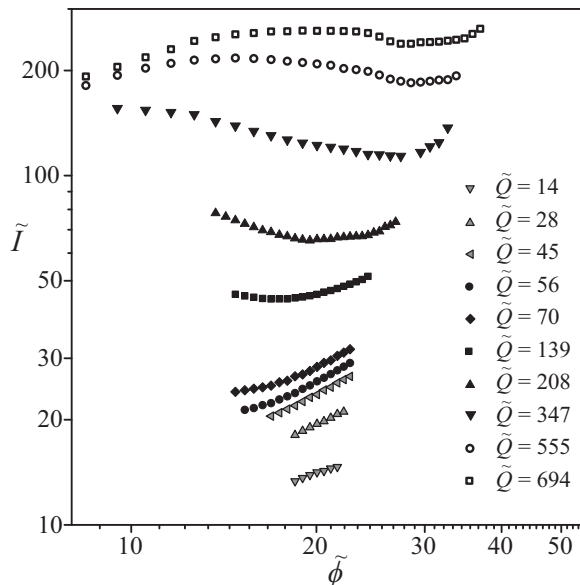


FIG. 5. Current characteristics of an EHD jet of 1-octanol for varying  $\tilde{\phi}$ , at the different values  $\tilde{Q}$  for a fixed aspect ratio  $\chi = 4$ . In the cone-jet regime ( $\tilde{Q} \lesssim 40$ ), the measured current  $\tilde{I}$  increases linearly with  $\tilde{\phi}$ . In the thick-jet regime at high  $\tilde{Q}$  and low  $\tilde{\phi}$ , the current increases linearly with  $\tilde{\phi}$ . At other conditions where the jet is moderately stretched, upon increasing the  $\tilde{\phi}$ , the current decreases, and thereafter it begins to increase with  $\tilde{\phi}$ .

increased, the thick-jet regime at  $\tilde{Q} = 694$  starts resembling the moderately stretched jet as observed at  $\tilde{Q} = 208$ .

Figure 5 shows the variation of the dimensionless current  $\tilde{I}$  with dimensionless applied potential difference  $\tilde{\phi}$  at a fixed aspect ratio of  $\chi = 4$  for various values of flow rate. At low flow rates ( $\tilde{Q} \lesssim 40$ ), where the cone-jet regime is observed, the current carried by the jet increases linearly with  $\tilde{\phi}$ . At intermediate flow rates ( $40 \lesssim \tilde{Q} \lesssim 500$ ), the current increases upon increasing  $\tilde{\phi}$  only at higher values of  $\tilde{\phi}$ . At lower values of  $\tilde{\phi}$ , the current varies slowly or even decreases with  $\tilde{\phi}$ . We will show later in Sec. III that such nonmonotonic variation of current with the applied potential difference is a characteristic of the moderately stretched jet regime, wherein conduction and surface convection currents are of comparable magnitude. At very high flow rates, for example, at  $\tilde{Q} = 694$ , the current increases with  $\tilde{\phi}$  for low values of  $\tilde{\phi}$ , whereas the current shows a nonmonotonic behavior at high values of  $\tilde{\phi}$  similar to that for a moderately stretched jet at intermediate flow rates. This is because, as shown in Fig. 4(c), the thick jet at  $\tilde{Q} = 694$  transitions to a moderately stretched jet upon increasing the potential difference.

#### D. Regimes of steady EHD jetting

The experimental visualization of the steady-jetting regimes of 1-octanol and the corresponding current measurements suggest that the steady EHD jetting can be classified into three regimes: (i) cone-jet, (ii) moderately stretched jet, and (iii) thick-jet. The distinction between these three regimes can be made based on the jet diameter and the length  $L_{ct}$  of the transition region (current transfer region) connecting the cone and the jet, and the current characteristics. The experimental observations suggest that these steady jetting regimes can depend even on the electric field, in addition to the flow rate. In particular, Eq. (3) suggests that for a given needle and liquid, the jetting regimes can depend on the dimensionless flow rate  $\tilde{Q}$ , the potential difference  $\tilde{\phi}$ , and the aspect ratio  $\chi$ . To identify the conditions for the existence of these regimes, in Fig. 6 we plot the operating



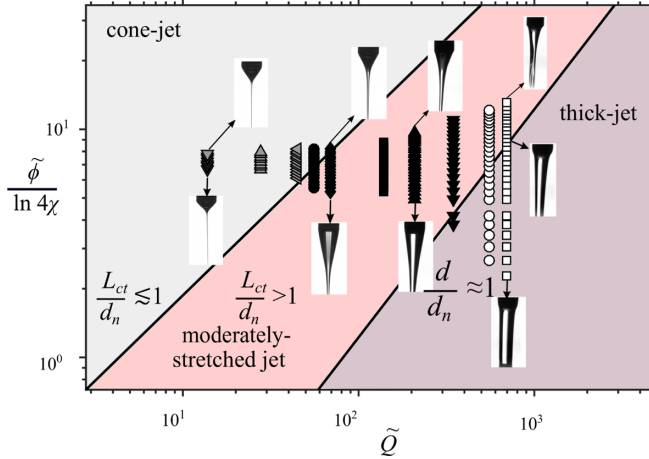


FIG. 6. Various regimes of an electrified jet of 1-octanol in the EHD jet printing configuration. An electrified jet shows three distinct regimes: (i) cone-jet regime, where the current transfer region is very small in comparison to the diameter of the needle,  $L_{ct}/d_n \lesssim 1$ , (ii) thick-jet regime, in which the diameter of the jet is approximately equal to the diameter of the needle,  $d \approx d_n$ , and (iii) moderately stretched jet regime, where the length of the current transfer region is the order of the needle diameter and needle to collector distance,  $L_{ct}/d_n \gtrsim 1$ , while the jet diameter is smaller than the needle diameter.

conditions at which we performed the experiments on a  $\tilde{\phi}/\ln 4\chi$  vs  $\tilde{Q}$  diagram. The data points in Fig. 6 correspond to the conditions for the current measurements shown in Fig. 5 with identical symbols. Also, the lines shown in Fig. 6 are the theoretically predicted boundaries separating the various regimes; the derivation of these limiting conditions is presented in Sec. III. Figure 6 enables a clear distinction between the three steady jetting regimes.

Figure 6 shows that the jetting occurs in the cone-jet mode at low flow rates. We note that, at low flow rates, steady jetting occurs over a narrow range of potential difference. Therefore, the transition between the cone jet and the moderately stretched jet depends primarily on the flow rate (at  $\tilde{Q} \approx 40$ ). The cone-jet regime is observed at ( $\tilde{Q} \lesssim 40$ ) and is characterized by a significantly small current transfer region compared with the needle diameter  $L_{ct}/d_n \lesssim 1$ . In this regime, the experiments show that current and jet diameter scale as  $\tilde{I} \sim \tilde{Q}^{1/2}$  and  $\tilde{d} \sim \tilde{Q}^{1/2}$ , respectively. While the current carried by the cone jet increases linearly with the potential difference  $\tilde{\phi}$ , the jet diameter does not vary appreciably with  $\tilde{\phi}$ .

Next, from Fig. 6 we observe that the thick-jet regime occurs at high flow rates and low values of  $\tilde{\phi}/\ln 4\chi$ . In this regime, the electrical stresses on the jet are not strong enough to stretch the jet. Consequently, the jet diameter remains similar to the needle diameter,  $d \approx d_n$ . The current carried by the thick jet remains nearly independent of the flow rate. Moreover, the jet's shape and diameter vary negligibly with the flow rate and applied potential. Note that the range of potential difference for steady jetting increases with the flow rate. Therefore, as shown in Fig. 6, at very high flow rates, the EHD jet can transition from a thick jet to moderately stretched jet by either decreasing the flow rate or increasing the potential difference. For the same reason, as shown in Fig. 5, the current at  $\tilde{Q} = 694$  shows the behavior of a thick jet at low  $\tilde{\phi}$  and that of a moderately stretched jet at higher values of  $\tilde{\phi}$ .

In between the cone-jet and thick-jet regimes on the  $\tilde{\phi}/\ln 4\chi$  vs  $\tilde{Q}$  diagram, the jet is moderately stretched as shown in Fig. 6. The cone-to-jet transition region for the moderately stretched jet is longer than the needle diameter but jet diameter is smaller than the needle diameter. In this regime, the current increases with the flow rate but exhibits a nonmonotonic behavior with the potential difference. The diameter of the moderately stretched jet scales as  $\tilde{d} \sim \tilde{Q}$ , as shown in Fig. 3(b).

Moreover, the jet shape and its diameter depend strongly on the potential difference, and the jet diameter reduces upon increasing  $\tilde{\phi}$ .

### III. SCALING ANALYSIS

Having described the various regimes of steady jetting in EHD jet printing through experiments for 1-octanol, we now present an order-of-magnitude analysis to estimate the criteria for various regimes and the scaling laws for jet diameter and current carried by the electrified jet. Our experimentally observed scaling behavior for the cone-jet regime is similar to the scaling relations for the cone jets in electrospray literature[11,17–20], where the collector is placed for from the needle. On the other hand, the scaling behavior of moderately stretched jet and thick-jet regimes has not been described earlier. Here we present order-of-magnitude analysis for moderately stretched and thick jet regimes wherein the axial variation of jet diameter is gradual, as opposed to the cone-jet regime.

We model the EHD jetting phenomenon observed in our experiments by approximating the metallic needle as a paraboloid,  $x = (d_n^2/4 - r^2)/d_n$ , where  $x$  and  $r$  denote axial and radial coordinates. This paraboloid has a circular cross section of diameter  $d_n$  at  $x = 0$ , and its tip is at  $x = d_n/4$ . The collector electrode is approximated as a confocal paraboloid at a distance of  $L$  from the needle tip, that is, at  $x = L + d_n/4$  for  $r = 0$ . The collector is grounded and a potential of  $\phi$  is applied to the needle. This needle-collector configuration admits an analytical expression for the electric potential in absence of the jet,  $\phi_\infty = \phi - A \ln\{2[\sqrt{x^2 + r^2} + x]/d_n\}$ , where  $A = \phi/\ln(1 + 4\chi)$ . In our experiments,  $\chi \geq 3$ , for which it is reasonable to approximate  $A$  as  $A \approx \phi/\ln 4\chi$ .

We consider a jet of leaky-dielectric liquid [8] flowing out of the paraboloid needle (truncated at  $x = 0$ ) under the effect of the applied electric field. A leaky-dielectric liquid is weakly conducting, and consequently, all the charges in the liquid are quickly conducted to the surface. Therefore, the charge is present only on the jet surface. This surface charge density  $\sigma$  modifies the external electric field  $\mathbf{E}_\infty = -\nabla\phi_\infty$ . Because there are no free charges away from the liquid surface, the electric fields inside and outside the liquid satisfy

$$\nabla \cdot \mathbf{E}_i = 0 \quad \text{and} \quad \nabla \times \mathbf{E}_i = 0, \quad i = 1, 2, \quad (4)$$

where subscripts 1 and 2 denote air and liquid, respectively. The tangential components of the electric field at the surface are equal  $E_{1t} = E_{2t}$  and are hereafter denoted as  $E_t$ . The normal component of electric fields ( $E_{1n}$  and  $E_{2n}$ ) at the jet surface are related to the surface charge density  $\sigma$  as

$$\sigma = \epsilon_1 E_{1n} - \epsilon_2 E_{2n}, \quad (5)$$

where  $\epsilon_1$  and  $\epsilon_2$  denote the permittivities of air and liquid, respectively. Because for a leaky-dielectric liquid  $\epsilon_2 E_{2n} \ll \epsilon_1 E_{1n}$  [28], the surface charge density is given by  $\sigma = \epsilon_0 E_{1n}$ , where we have considered that the permittivity of air ( $\epsilon_1$ ) is equal to the permittivity of free space ( $\epsilon_0$ ). The coupling between this surface charge and electric field results in electrical stresses on the liquid surface.

To model the fluid flow, we consider a steady flow of a leaky-dielectric liquid, assuming that the jet radius  $r = r(x)$  varies slowly along the axial direction  $x$ . The governing equations for quasi-one-dimensional, steady-state EHD jetting of a leaky-dielectric liquid, incorporating the electric stresses and interfacial tension, have been derived earlier by Feng [13] and are given as

$$\pi r^2 v = Q \quad (6)$$

and

$$\frac{d}{dx} \left( \frac{\rho v^2}{2} \right) = \rho g + \frac{3}{r^2} \frac{d}{dx} \left( \mu r^2 \frac{dv}{dx} \right) + \frac{2\sigma E_t}{r} + \frac{d}{dx} \left[ \frac{\sigma^2}{2\epsilon_0} - \frac{\gamma}{r} + \frac{\epsilon_0(\epsilon_r - 1)E_t^2}{2} \right]. \quad (7)$$

Here  $v$  denotes the axial velocity,  $\rho$  the density,  $\mu$  the dynamic viscosity,  $\gamma$  the interfacial tension, and  $\epsilon_r = \epsilon_2/\epsilon_0$  the relative permittivity of the liquid. Equation (6) models the conservation of mass

and relates the jet radius  $r$  with the axial velocity  $v$ , which is assumed to be uniform across the jet cross section. Equation (7) is the momentum equation, wherein the left-hand side term corresponds to inertia, while the terms on the right-hand side represent gravity, viscous resistance, tangential electric force, electrostatic suction, surface tension, and polarization force, respectively. Next, charge conservation at any axial location along the jet gives the total current  $I$ ,

$$\pi r^2 k E_t + 2\pi r \sigma v = I. \quad (8)$$

The total current  $I$  is a constant for steady jetting. The first and second terms on the left-hand side of Eq. (8) represent the conduction current  $I_b$  and the surface convection current  $I_s$ , respectively.

Equipped with the governing equations for an electrified jet, we now perform scaling analysis to estimate the criteria for various jetting regimes and the corresponding scaling laws for current. The various regimes for steady EHD jetting can be distinguished based on the length of the current transfer region connecting the cone and jet, and the jet diameter. Therefore, we apply the governing equations to the current transfer region where the conduction and convection currents are of comparable magnitude  $I_b \sim I_s$ . We denote the length of the current transfer region as  $L_{ct}$  and the jet diameter in this region as  $d_{ct}$  [11]. When the current transfer region is smaller than the nozzle-to-collector distance  $L$ , the reference scale for the tangential component of the electric field can be taken as  $E_t \sim A/L_{ct}$ . This scaling of the tangential electric field is applicable only for a slender jet with a gradual axial variation of the jet diameter. This is in contrast to the cone-jet regime, where the tangential electric field is governed by the electric field due to the Taylor cone [21,27]. Given that  $E_t \sim A/L_{ct}$ , noting that the electric field is irrotational [Eq. (4)], we arrive at the reference scales for normal electric field and the surface charge density,

$$E_{1n} \sim \frac{L_{ct}}{d_{ct}} E_t \quad \text{and} \quad \sigma = \epsilon_0 E_{1n} \sim \frac{L_{ct}}{d_{ct}} \epsilon_0 E_t \sim \epsilon_0 \frac{A}{d_{ct}}. \quad (9)$$

The jet velocity  $v$  in the current transfer region scales as  $v \sim Q/d_{ct}^2$ , from the mass conservation Eq. (6). The conduction and convection currents scale as  $I_b \sim k d_{ct}^2 E_t \sim k d_{ct}^2 A/L_{ct}$  and  $I_s \sim \sigma d_{ct} v \sim A \epsilon_0 Q/d_{ct}^2$ , respectively. We can now relate  $L_{ct}$  and  $d_{ct}$  noting that  $I_b \sim I_s$  in current transfer region, which gives

$$L_{ct} \sim \frac{k d_{ct}^4}{Q \epsilon_0}. \quad (10)$$

Finally, we use the momentum equation (7) to obtain explicit scaling relations for  $L_{ct}$  and  $d_{ct}$  in terms of operating conditions and liquid properties. To this end, we assume that the gravity, viscous, and polarization forces are negligible. Moreover, the force due to interfacial tension is balanced by the electrostatic suction forces [see Eq. (7)]. Therefore, we assume that the EHD jet primarily stretches and accelerates due to the tangential electric force in the current transfer region. The range of validity of this assumption is discussed in Sec. IV. By balancing the inertia and tangential electric force terms in Eq. (7),  $\rho v^2/L_{ct} \sim \sigma E_t/d_{ct}$ , and using the scaling relations for various quantities derived above, we arrive at the characteristic scales for the diameter  $d_{ct}$  and the length  $L_{ct}$  of the current transfer region,

$$d_{ct} \sim Q \rho^{1/2} / (A \epsilon_0^{1/2}) \quad \text{and} \quad L_{ct} \sim k \rho^2 Q^3 / (\epsilon_0^3 A^4). \quad (11)$$

Based on the order-of-magnitudes of  $L_{ct}$  and  $d_{ct}$ , we can classify steady EHD jetting into three distinct regimes.

### A. Cone-jet regime

The cone-jet regime occurs at low flow rates, as observed in our experiments (see Fig. 6). This regime is similar to the well-known Taylor cone-jet regime routinely observed in the far-field EHD jetting process [19,21,29]. In this regime, the tangential electric forces are large enough to stretch the meniscus into a fine jet,  $d/d_n \ll 1$ . Moreover, the cone-jet transition is sufficiently local, which

results in a small current transfer region compared with the needle diameter,  $L_{ct}/d_n \lesssim 1$ , as can be seen in Fig. 2(i) and 2(ii). As shown in Fig. 6, in our experiments, the condition  $L_{ct}/d_n \lesssim 1$  also ensures that the jet diameter is small. Therefore, using the expression of  $L_{ct}$  from Eq. (11) in  $L_{ct}/d_n \lesssim 1$ , we arrive at the criterion for the cone-jet regime,

$$\tilde{Q} \lesssim \left(\frac{d_n}{d_0}\right)^{1/3} \left(\frac{\tilde{\phi}}{\ln 4\chi}\right)^{4/3}. \quad (12)$$

For a typical value of  $\tilde{\phi}/\ln 4\chi = 5$  as in our experiments, this criterion gives  $\tilde{Q} \lesssim 37$ , which is in agreement with the condition of  $\tilde{Q} \lesssim 40$  observed in our experiments [see Figs. 3(a) and 3(b)].

While the criterion given by Eq. (12) for observing the cone-jet regime is specific to the EHD jet printing configuration, the scaling relations law of current and jet diameter are the same as those observed for Taylor cone jet in electrospray. These scaling relations have been derived earlier by Gañán-Calvo [14,17]. As shown by Gañán-Calvo [14], the jet diameter scales as the square root of the flow rate,  $d \sim Q^{1/2}$ . In the cone-jet regime, the total current downstream of the narrow current transfer region is dominated by surface convection, that is,  $I \sim I_s \sim \sigma Q/d$ . Because  $d \sim Q^{1/2}$ , the total current also scales as  $I \sim Q^{1/2}$  [17,19,21,29,30]. As shown in Fig. 3, our experiments show the same scaling behavior for current and jet diameter.

### B. Thick-jet regime

The thick-jet regime is observed at high flow rates and low potential difference  $\tilde{\phi}$ , as shown in Fig. 6. In this regime, inertia dominates over the tangential electric force, and consequently, the jet is negligibly stretched. Therefore, the jet remains thick, and its diameter is comparable to the needle diameter,  $d \approx d_n$ , as can be seen from Fig. 2(vi) and 2(vii). We obtain the criterion for the onset of the thick-jet regime by setting  $d_{ct}/d_n \gtrsim 1$ , which yields

$$\tilde{Q} \gtrsim \left(\frac{d_n}{d_0}\right) \left(\frac{\tilde{\phi}}{\ln 4\chi}\right). \quad (13)$$

For a typical value of  $\tilde{\phi}/\ln 4\chi \sim 5$  as in our experiments, this condition simplifies to  $\tilde{Q} \gtrsim 409$ , which is consistent with our experiments wherein a thick jet is observed for  $\tilde{Q} \gtrsim 500$  (see Fig. 6).

In this regime, the scaling law for current can be determined by noting that the jet diameter is approximately equal to needle diameter,  $d \approx d_n$ . The length of the current transfer region in this regime can be estimated by replacing  $d_{ct}$  with  $d_n$  in Eq. (10), which gives  $L_{ct} \sim kd_n^4/(\epsilon_0 Q)$ . For our experiments with 1-octanol,  $L_{ct}/d_n \sim (1/\tilde{Q})(d_n/d_0)^3 \sim O(10^3)$ , which is significantly larger than the aspect ratio  $L/d_n \sim O(1)$ . This suggests that the applied potential  $\phi$  drops across the needle-to-collector distance  $L$  rather than  $L_{ct}$ . Therefore, scaling the tangential electric field as  $A/L$ , the conduction current scales as  $I_b \sim kd_n^2 E_t \sim kd_n^2 A/L$  and surface convection current scales as  $I_s \sim \sigma d_n v \sim \epsilon_0 A Q/d_n^2$ . The ratio of these two currents  $I_b/I_s \sim kd_n^4/(L\epsilon_0 Q) \sim L_{ct}/L$ . Because  $L_{ct} \gg L$  in near-electrode configuration of our experiments, the surface convection current is negligible. Therefore, the total current  $I \sim I_b$  and given as

$$\tilde{I} \sim \frac{\tilde{\phi}}{\ln 4\chi} \left(\frac{d_n}{d_0}\right) \left(\frac{1}{\chi}\right). \quad (14)$$

This scaling shows that total current is independent of  $\tilde{Q}$  and depends only on  $\tilde{\phi}$  and  $\chi$  in the thick-jet regime. The scaling of thick jet regime also corroborates with our experimental observation of 1-octanol at high  $\tilde{Q}$  for low values of  $\tilde{\phi}$  [see Fig. 3(a) and Fig. 5], wherein the current asymptotes to a constant value.

To further validate the scaling relation for the current in the thick jet regime, we performed additional experiments for varying values of  $\chi$  and  $\tilde{\phi}$  at a high flow rate of  $\tilde{Q} = 833$  for which jetting occurs in the thick-jet regime. Figure 7 shows the variation of dimensionless current  $\tilde{I}$  with  $\tilde{\phi}/\ln 4\chi$  for varying values of the aspect ratio  $\chi$ . The measured current increases linearly with

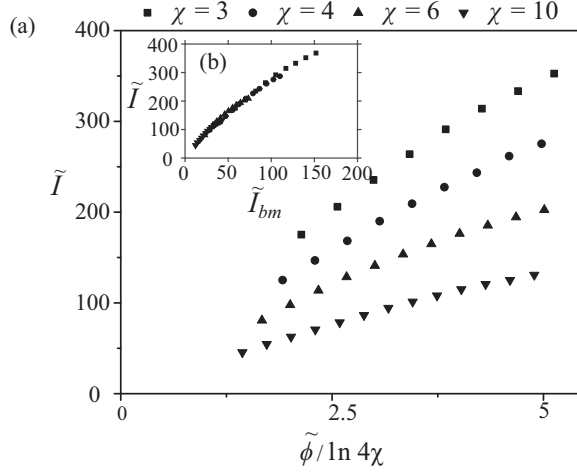


FIG. 7. The dependence of the measured current on the aspect ratio  $\chi$  in the thick jet regime for 1-octanol at  $\tilde{Q} = 833$  at low  $\tilde{\phi}$ . (a) The dimensionless current  $\tilde{I}$  scales linearly with  $\tilde{\phi} / \ln 4\chi$  in this regime at various  $\chi$ . In the inset, (b)  $\tilde{I}$  is plotted against  $\tilde{I}_{bm}$  collapses in a single curve, which validates Eq. (14). Here  $\tilde{I}_{bm}$  is the total current in the thick jet regime predicted by Eq. (14).

$\tilde{\phi} / \ln 4\chi$  for varying values of  $\chi$  as predicted by Eq. (14). Moreover, the measured current increases at a faster rate with  $\tilde{\phi}$  for low aspect ratios as predicted by Eq. (14). When the data are plotted on  $\tilde{I}$  vs  $\tilde{I}_{bm}$ , where  $\tilde{I}_{bm} = [\tilde{\phi} / \ln(4\chi)](d_n/d_0)(1/\chi)$  is the right-hand side of Eq. (14), all the data points collapse in a single curve, which validates Eq. (14).

Note that our scaling for the thick-jet regime differs from the scaling proposed by Higuera [11] through numerical simulations of EHD jetting in far-electrode configuration. In the far-electrode configuration simulated by Higuera [11],  $L/d_n \gg 1$  and  $L_{ct} \ll L$ . Therefore, surface convection dominates downstream in the thick jet simulated by Higuera. In near-electrode configuration as in our experiments,  $L_{ct} \ll L$  for a thick jet would occur at impractically high flow rates given by  $L_{ct} \sim kd_n^4/(\epsilon_0 Q) \ll 1$ , at  $\tilde{Q} > O(10^5)$ .

### C. Moderately stretched jet regime

The experimental observations, consolidated in Fig. 6, suggest a third regime with a moderately stretched jet that either occurs at intermediate flow rates or at high flow rates and high potential difference. In contrast to the cone-jet regime, complete current transfer does not occur in the moderately stretched jet regime. Also, unlike the thick jet, the moderately stretched jet has a smaller diameter than the needle diameter. As shown in Fig. 2(iv) and 2(v), in this regime the cone-to-jet transition is incomplete. Moreover, the tangential electric force is stronger in this case compared with that for the thick-jet regime. Consequently, the moderately stretched regime occurs when the conditions given by Eqs. (12) and (13) for cone jet and thick jet are not satisfied. Therefore, the criterion for moderately stretched jet regime is given by

$$\left(\frac{d_n}{d_0}\right)^{1/3} \left(\frac{\tilde{\phi}}{\ln 4\chi}\right)^{4/3} \lesssim \tilde{Q} \lesssim \left(\frac{d_n}{d_0}\right) \left(\frac{\tilde{\phi}}{\ln 4\chi}\right). \quad (15)$$

Figure 6 shows that the theoretical criteria for transition between the three jetting regimes agree well with experimental observations.

The scaling relation for current in the moderately stretched regime can be derived, noting that in this regime the order-of-magnitude estimate of the  $L_{ct}$  obtained from Eq. (11) can exceed the needle-to-collector distance  $L$ . Therefore, the conduction and surface convection currents are of comparable

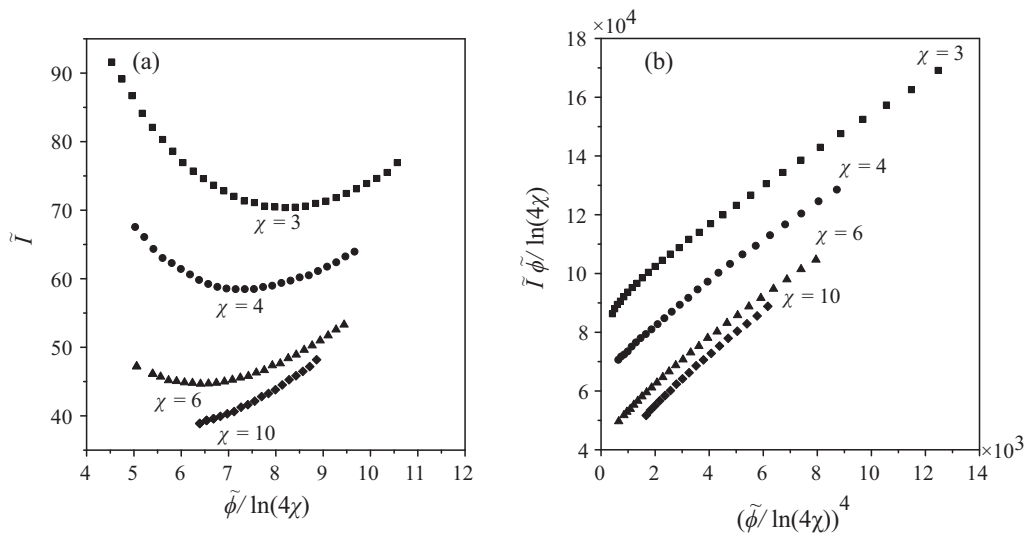


FIG. 8. The dependence of measured current on the aspect ratio  $\chi$  in the moderately stretched jet regime for 1-octanol at  $\tilde{Q} = 208$ . (a) The dimensionless current  $\tilde{I}$  shows a nonmonotonic dependence on  $\tilde{\phi}/\ln 4\chi$ , which is in qualitative agreement with Eq. (16). (b) Replotting the data on a  $\tilde{I}\tilde{\phi}/\ln 4\chi$  vs  $(\tilde{\phi}/\ln 4\chi)^4$  plot shows that the intercept, corresponding to the conduction current, decreases upon increasing  $\chi$ , as predicted by Eq. (17).

magnitude,  $I_b \sim I_s$  throughout the moderately stretched jet. This is in contrast to the cone-jet and thick-jet regimes, where surface convection and conduction currents, respectively, dominate downstream of the jet. Consequently, for the moderately stretched jet, the applied potential  $\phi$  also drops across the needle-to-collector distance  $L$  rather than  $L_{ct}$ , the appropriate scale for tangential electric field in a moderately stretched jet is  $A/L$  rather than  $A/L_{ct}$ . Therefore, the conduction current scales as  $I_b \sim kd_{ct}^2 E_t \sim \rho k Q^2 / (\epsilon_0 A L)$  and surface convection current scales as  $I_s \sim \sigma d_{ct} v \sim \epsilon_0^2 A^3 / (\rho Q)$ . The total current  $I = I_b + I_s \sim \rho k Q^2 / (\epsilon_0 A L) + \epsilon_0^2 A^3 / (\rho Q)$  in dimensionless form is given by

$$\tilde{I} \sim \frac{\tilde{Q}^2}{(\tilde{\phi}/\ln 4\chi)} \left( \frac{d_0}{d_n} \right) \frac{1}{\chi} + \frac{1}{\tilde{Q}} \left( \frac{\tilde{\phi}}{\ln 4\chi} \right)^3. \quad (16)$$

The first and second terms on the right-hand side of this relation respectively represent the contribution of conduction and surface convection currents to the total current. Note that the conduction and surface convection currents scale with the potential difference as  $I_b \sim 1/\tilde{\phi}$  and  $I_s \sim \tilde{\phi}^3$ . Therefore, as  $\tilde{\phi}$  is progressively increased, keeping the flow rate and aspect ratio fixed, the total current first decreases and subsequently starts increasing. Similar nonmonotonic dependence of current on applied potential difference is observed for a moderately stretched jet in our experiments, as shown in Fig. 5. Note that, for a moderately stretched jet, the conduction and surface convection currents are of comparable magnitude. Therefore,  $I_b \sim 1/\tilde{\phi}$  and  $I_s \sim \tilde{\phi}^3$  scaling relations cannot be identified individually from the measurements of total current.

The moderately stretched jet regime differs from the cone jet because the characteristic length scale over which voltage drops is the needle-to-substrate distance  $L$ , instead of  $L_{ct}$ . For the same reason, the conduction current term in the scaling relation for current, Eq. (16), depends on the aspect ratio  $\chi$ . To validate this dependence of current on the aspect ratio  $\chi$ , we measured the current carried by the moderately stretched jet of 1-octanol for varying values of  $\chi$  and  $\tilde{\phi}$ . Figure 8(a) shows the variation of dimensionless current  $\tilde{I}$  with  $\tilde{\phi}/\ln 4\chi$  at a fixed flow rate of  $\tilde{Q} = 208$  for various values of the aspect ratio  $\chi$ . The total current exhibits a nonmonotonic dependence on  $\tilde{\phi}/\ln 4\chi$  for  $\chi = 3, 4$ , and  $6$ , as predicted by Eq. (16). Moreover, for a fixed value of  $\tilde{\phi}/\ln 4\chi$ , Fig. 8(a)

shows that the total current decreases upon increasing the aspect ratio  $\chi$  because of the  $I_b \sim 1/\chi$  dependence of the conduction current.

To further elucidate the dependence of current on the aspect ratio, we rewrite Eq. (16) as

$$\tilde{I}(\tilde{\phi}/\ln 4\chi) \sim \tilde{Q}^2 \left( \frac{d_0}{d_n} \right) \frac{1}{\chi} + \frac{1}{\tilde{Q}} \left( \frac{\tilde{\phi}}{\ln 4\chi} \right)^4, \quad (17)$$

and replot the data presented in Fig. 8(a) in Fig. 8(b) on a  $\tilde{I}\tilde{\phi}/\ln 4\chi$  vs  $(\tilde{\phi}/\ln 4\chi)^4$  plot. As predicted by Eq. (17), the experimental data for a fixed flow rate of  $\tilde{Q} = 208$  fall on straight lines. In particular, the slopes of these lines for different  $\chi$  are equal, because the coefficient of  $(\tilde{\phi}/\ln 4\chi)^4$  term (corresponding to the surface convection current) in Eq. (17) does not depend on  $\chi$ . Also, the experimental data show that the intercepts of the straight lines decrease upon increasing the aspect ratio. This is in agreement with the  $1/\chi$  dependence of the intercept in Eq. (17), which corresponds to the conduction current. Therefore, the current measurements presented in Fig. 8(b) provide a conclusive validation of the aspect-ratio dependence of current, given by Eq. (16). Moreover, this validation of Eq. (16) shows that the current is not completely transferred from conduction to surface current in the moderately stretched regime.

Lastly, we note that the diameter of the moderately stretched jet scales with the diameter of the current transfer region. Therefore, from Eq. (11),  $d \sim d_{ct} \sim (Q/A)(\rho/\epsilon_0)^{\frac{1}{2}}$ . This linear dependence of jet diameter with the flow rate is also observed in the experiments at intermediate flow rates, as shown in Fig. 3(b). For a typical value of  $\tilde{Q} = 208$ ,  $\tilde{\phi} = 18.9$ , and  $\chi = 3$  as in our experiments, the calculated value of jet diameter ( $d_{ct}/d_0 = 27.3$ ) is in qualitative agreement with the measured value of jet diameter as shown in Fig. 3(b). Overall, Fig. 6 shows that the criteria for jetting to occur in various regimes, obtained through order-of-magnitude analysis, agree well with those obtained experimentally. Moreover, the theoretical scaling relations for current and diameter for the three regimes are consistent with the scaling behavior observed in experiments.

#### IV. THE LIMITS OF VALIDITY OF THE SCALING RELATIONS

The scaling analysis presented in Sec. III is based on the balance of inertia and tangential electrostatic force terms in the momentum equation, Eq. (7). That is, we have neglected the viscous forces and the axial component of the polarization force in our analysis. This assumption is valid for our experiments with 1-octanol, wherein the Reynolds number  $Re = \rho v d / \mu$  and  $Re_0$  based on the reference velocity and diameter scales is  $O(1)$ . In addition, for the scaling analysis, we have assumed that the axial electrostatic force due to the coupling of free charge on the surface and the tangential electric field dominates the force due to the polarization charges. This assumption can be justified by considering the ratio of tangential electrostatic and polarization forces in the momentum equation, Eq. (7),

$$\frac{2\sigma E_t/r}{d/dx[\epsilon_0(\epsilon_r - 1)E_t^2/2]} \sim \frac{\epsilon_0 E_n E_t / d_{ct}}{\epsilon_0(\epsilon_r - 1)E_t^2 / L_{ct}} \sim \left( \frac{L_{ct}}{d_{ct}} \right)^2 \frac{1}{(\epsilon_r - 1)}. \quad (18)$$

For slender jets with  $L_{ct} \gg d_{ct}$ , the above relation shows that the polarization force is dominant only for highly polar liquids [ $\epsilon_r \sim O(100)$ ]. For liquids with relative permittivity  $\epsilon_r \sim O(10)$ , such as 1-octanol, the polarization force can be neglected. We also note that, far downstream of a fully developed jet, the tangential electrostatic force is the only positive driving force [17].

For a steady cone jet, wherein the length of the current transfer region is significantly smaller than the nozzle diameter, Gañán-Calvo [17] has shown that the viscous and polarization forces can be neglected if

$$\tilde{Q} \gg \left( \frac{\tilde{Q}}{Re_0} \right)^{1/4} \quad \text{and} \quad \frac{\tilde{Q}}{(\epsilon_r - 1)} \gg 1, \quad (19)$$

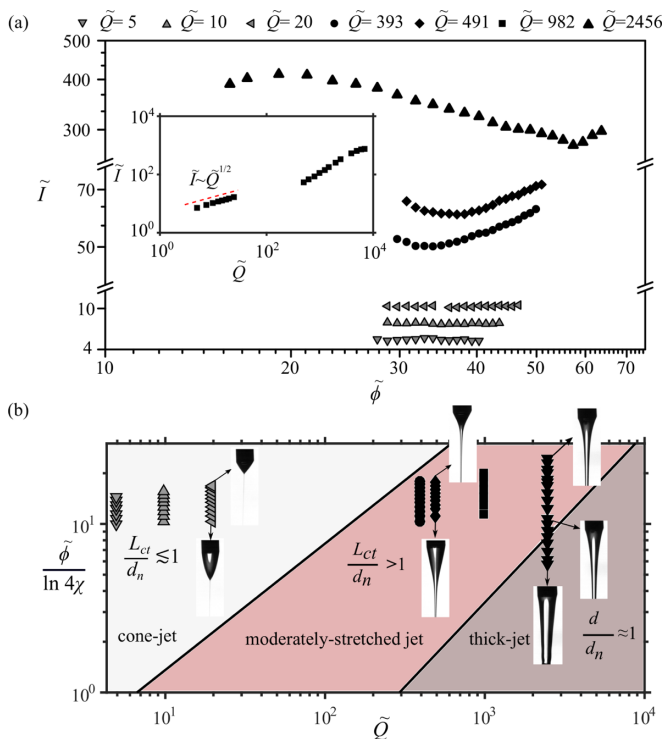


FIG. 9. Current characteristics of an EHD jet of 1-butanol for varying operating parameters ( $\tilde{Q}$  and  $\tilde{\phi}$ ). (a) Dimensionless current  $\tilde{I}$  vs dimensionless applied potential difference  $\tilde{\phi}$  for various dimensionless flow rates  $\tilde{Q}$  at  $\chi = 4$ . The inset of (a) shows  $\tilde{I}$  vs  $\tilde{Q}$  for fixed  $\tilde{\phi} = 32$  and  $\chi = 4$ . (b) Various regimes of EHD jetting of 1-butanol in the printing configuration. EHD jetting of 1-butanol shows similar behavior as that for 1-octanol.

respectively. For typical values of  $\tilde{Q} = 20$ ,  $\text{Re}_0 = 2.0$ , and  $\epsilon_r = 10.3$  for steady cone-jet experiments of 1-octanol presented here, these conditions are not violated. This is consistent with the observations of Gañán-Calvo [17] that steady cone jetting in 1-octanol is dominated by inertia and electrostatic suction, and not by viscous and polarization forces.

Typically, a large majority of liquids exhibit EHD jetting dominated by inertia and electrostatic force. Viscous forces dominate only in EHD jetting of highly viscous liquids such as glycerol ( $\mu = 1.4 \text{ Pa s}$ ) and polarization force dominates for highly polar liquids such as formamide ( $\epsilon_r = 111$ ) [17]. To demonstrate that our scaling analysis is not limited to 1-octanol, we performed another set of experiments with 1-butanol. Similar to 1-octanol, EHD jetting of 1-butanol is dominated by inertia and electrostatic force. Measurements of current carried by the EHD jets of 1-butanol for  $\chi = 4$ , presented in Fig. 9(a), show similar  $\tilde{I}$  vs  $\tilde{\phi}$  behavior as that for 1-octanol. The moderately stretched EHD jets of 1-butanol also exhibit nonmonotonic dependence of current on the applied potential difference. As discussed in Sec. III C, such nonmonotonic dependence of current with applied potential difference is specific to EHD jet printing process where the jet is not long enough for conduction current to completely transform to surface convection current downstream of the jet. The inset of Fig. 9(a) shows the variation of measured  $\tilde{I}$  with  $\tilde{Q}$  at fixed  $\tilde{\phi} = 32$  and  $\chi = 4$ . Similar to 1-octanol, EHD jetting of 1-butanol exhibits  $\tilde{I} \sim \tilde{Q}^{1/2}$  scaling at low flow rates. Moreover,  $\tilde{I}$  asymptotes to a constant value at high flow rates. Note that, the current measurements are not shown for  $\tilde{Q} = 25\text{--}400$  in the inset because stable jetting was not observed for these flow rates at  $\tilde{\phi} = 32$ . Lastly, to validate the criteria for jetting to occur in various regimes, in Fig. 9(b) we plot the operating conditions for EHD jetting experiments for 1-butanol along with the theoretical limits



for various regimes derived in Sec. III. Similar to that data for 1-octanol presented in Fig. 6, the theoretical criteria to distinguish various regimes of stable EHD jetting also agree well with the experimental observations for 1-butanol.

## V. CONCLUSION

We have described the various regimes of steady jetting in the EHD jet printing process, wherein a liquid jet issuing from a needle is stretched by applying high electric field between the needle and the collector substrate. Although EHD jetting is well known in the context of the electrospray process, we have shown through experiments and theoretical scaling analysis that the jetting characteristics can differ significantly in the printing configuration, in which the needle is kept close to the collector. In particular, we have focused on the EHD jetting of the liquids for which the viscous and polarization forces are negligible compared to inertia and the tangential electric force, respectively. Through experimental visualization of the EHD jetting process and current measurements, we have shown that steady EHD jetting can occur in three regimes, namely, the cone-jet, moderately stretched jet, and thick-jet regimes.

The cone-jet regime is observed at low flow rates and is characterized by a thin jet streaming from the tip of the conical liquid meniscus attached to the needle. This regime is similar to the cone-jet regime in the electrospray process and exhibits well-known dependence of current and jet diameter with the square root of the flow rate. The thick-jet regime is observed at high flow rates and low applied electric field. In this regime, the electric forces are not strong enough to stretch and thin the jet. Consequently, the jet diameter is comparable to the needle diameter. The current carried by the thick jet is primarily due to bulk conduction and scales linearly with the applied potential difference. At other conditions for steady jetting, a moderately stretched jet is observed whose diameter scales linearly with the flow rate. Although the current carried by the moderately stretched jet increases with the flow rate, this regime exhibits nonmonotonic behavior of current with the applied potential. While the cone jet is observed in the electrospray process, the moderately stretched jet and thick jet regimes are specific to the EHD jet printing process, as the jet is not long enough for the conduction current, which dominates upstream, to completely transform to surface convection current downstream of the jet.

To supplement the experimental observations, we have also performed order-of-magnitude analysis to elucidate the underlying physics of these experimentally observed regimes. Based on the relative size of the current transfer region and the jet diameter, we have derived the conditions in terms of operating parameters (flow rate, applied potential, and aspect ratio) for observing the three regimes. For each of these regimes, we have also described the dependence of the jet diameter and the current carried by jet on flow rate, potential difference, and aspect ratio in the form of scaling relations. The theoretical criteria for observing various regimes and the corresponding scaling behavior of jet diameter and current are in agreement with the experimental observations. The experimentally validated criteria for various jetting regimes can help in reducing the preliminary experimental trials to find the right operating conditions for EHD jet printing. Moreover, the scaling laws for jet diameter and current can be useful for design, performance monitoring, and control of EHD jet printing.

This work focused on the EHD jetting due to dominant inertia and the tangential electric force. While a majority of liquids exhibit EHD jetting dominated by inertia and tangential electric force, viscous and polarization forces may dominate for certain liquids. A natural extension of the current work would be to apply the current approach to investigate EHD jetting in the printing configuration for liquids with dominant viscous and polarization forces.

## ACKNOWLEDGMENTS

We acknowledge the financial support received from the Science and Engineering Research Board (SERB), Government of India, under the Impacting Research Innovation and Technology

(IMPRINT-2) Scheme (Grant No. IMP/2018/000422). We also acknowledge the funding received from IIT Delhi under the Faculty Interdisciplinary Research Project (FIRP) scheme.

- [1] J. U. Park, M. Hardy, S. J. Kang, K. Barton, K. Adair, D. K. Mukhopadhyay, C. Y. Lee, M. S. Strano, A. G. Alleyne, J. G. Georgiadis *et al.*, High-resolution electrohydrodynamic jet printing, *Nat. Mater.* **6**, 782 (2007).
- [2] M. S. Onses, E. Sutanto, P. M. Ferreira, A. G. Alleyne, and J. A. Rogers, Mechanisms, capabilities, and applications of high-resolution electrohydrodynamic jet printing, *Small* **11**, 4237 (2015).
- [3] Y. Kim, S. Jang, and J. H. Oh, High-resolution electrohydrodynamic printing of silver nanoparticle ink via commercial hypodermic needles, *Appl. Phys. Lett.* **106**, 014103 (2015).
- [4] Y. Jang, I. Hartarto Tambunan, H. Tak, V. Dat Nguyen, T. Kang, and D. Byun, Non-contact printing of high aspect ratio Ag electrodes for polycrystalline silicone solar cell with electrohydrodynamic jet printing, *Appl. Phys. Lett.* **102**, 123901 (2013).
- [5] S. H. Ahn, H. J. Lee, and G. H. Kim, Polycaprolactone scaffolds fabricated with an advanced electrohydrodynamic direct-printing method for bone tissue regeneration, *Biomacromolecules* **12**, 4256 (2011).
- [6] V. Vespini, S. Coppola, M. Todino, M. Paturzo, V. Bianco, S. Grilli, and P. Ferraro, Forward electrohydrodynamic inkjet printing of optical microlenses on microfluidic devices, *Lab Chip* **16**, 326 (2016).
- [7] E. Sutanto, Y. Tan, M. S. Onses, B. T. Cunningham, and A. Alleyne, Electrohydrodynamic jet printing of micro-optical devices, *Manuf. Lett.* **2**, 4 (2014).
- [8] D. Saville, Electrohydrodynamics: The Taylor-Melcher leaky dielectric model, *Annu. Rev. Fluid Mech.* **29**, 27 (1997).
- [9] M. Cloupeau and B. Prunet-Foch, Electrostatic spraying of liquids in cone-jet mode, *J. Electrostat.* **22**, 135 (1989).
- [10] M. Cloupeau and B. Prunet-Foch, Electrostatic spraying of liquids: Main functioning modes, *J. Electrostat.* **25**, 165 (1990).
- [11] F. Higuera, Electric current of an electrified jet issuing from a long metallic tube, *J. Fluid Mech.* **675**, 596 (2011).
- [12] K. Barton, S. Mishra, A. Alleyne, P. Ferreira, and J. Rogers, Control of high-resolution electrohydrodynamic jet printing, *Cont. Eng. Prac.* **19**, 1266 (2011).
- [13] J. Feng, The stretching of an electrified non-Newtonian jet: A model for electrospinning, *Phys. Fluids* **14**, 3912 (2002).
- [14] A. M. Gañán-Calvo and J. M. Montanero, Revision of capillary cone-jet physics: Electro spray and flow focusing, *Phys. Rev. E* **79**, 066305 (2009).
- [15] S. V. Fridrikh, H. Y. Jian, M. P. Brenner, and G. C. Rutledge, Controlling the Fiber Diameter during Electrospinning, *Phys. Rev. Lett.* **90**, 144502 (2003).
- [16] C. Wang, C. H. Hsu, and J. H. Lin, Scaling laws in electrospinning of polystyrene solutions, *Macromolecules* **39**, 7662 (2006).
- [17] A. M. Gañán-Calvo, On the general scaling theory for electro spraying, *J. Fluid Mech.* **507**, 203 (2004).
- [18] F. Higuera, Flow rate and electric current emitted by a Taylor cone, *J. Fluid Mech.* **484**, 303 (2003).
- [19] J. F. De La Mora and I. G. Loscertales, The current emitted by highly conducting Taylor cones, *J. Fluid Mech.* **260**, 155 (1994).
- [20] A. M. Gañán-Calvo, Cone-Jet Analytical Extension of Taylor's Electrostatic Solution and the Asymptotic Universal Scaling Laws in Electro spraying, *Phys. Rev. Lett.* **79**, 217 (1997).
- [21] A. Gañán-Calvo, J. Davila, and A. Barrero, Current and droplet size in the electro spraying of liquids. Scaling laws, *J. Aerosol. Sci.* **28**, 249 (1997).
- [22] M. M. Hohman, M. Shin, G. Rutledge, and M. P. Brenner, Electrospinning and electrically forced jets. II. Applications, *Phys. Fluids* **13**, 2221 (2001).
- [23] F. Higuera, Current/flow-rate characteristic of an electro spray with a small meniscus, *J. Fluid Mech.* **513**, 239 (2004).

- [24] J. Fernández de la Mora, The fluid dynamics of Taylor cones, *Annu. Rev. Fluid Mech.* **39**, 217 (2007).
- [25] G. Riboux, A. G. Marin, I. G. Loscertales, and A. Barrero, Whipping instability characterization of an electrified visco-capillary jet, *J. Fluid Mech.* **671**, 226 (2011).
- [26] S. S. Bahga, *Experimental Uncertainty Analysis: A Textbook for Science and Engineering Students* (White Falcon, New Delhi, 2021).
- [27] A. Ponce-Torres, N. Rebollo-Muñoz, M. Herrada, A. Gañán-Calvo, and J. Montanero, The steady cone-jet mode of electrospinning close to the minimum volume stability limit, *J. Fluid Mech.* **857**, 142 (2018).
- [28] A. M. Ganan-Calvo, On the theory of electrohydrodynamically driven capillary jets, *J. Fluid Mech.* **335**, 165 (1997).
- [29] P. Bhattacharjee, T. M. Schneider, M. Brenner, G. H. McKinley, and G. C. Rutledge, On the measured current in electrospinning, *J. Appl. Phys.* **107**, 044306 (2010).
- [30] W. Li, X. Wang, G. Zheng, L. Xu, J. Jiang, Z. Luo, S. Guo, and D. Sun, Current characteristics of stable cone-jet in electrohydrodynamic printing process, *Appl. Phys. A* **124**, 711 (2018).